A Systematic Resolution Study of $\tau\tau$ Decays at CMS at the LHC

by

Ryan Howard Foote

Submitted to the Department of Physics
in partial fulfillment of the requirements for the degree of

Bachelor of Science in Physics

at the

MASSACHUSETTS INSTITUTE OF TECHNOLOGY

June 2011

Author .....
Department of Physics
May 20, 2011

Certified by.... .....
Markus Klute
Assistant Professor
Thesis Supervisor

Accepted by .....
Professor Nergis Mavalvala
Senior Thesis Coordinator, Department of Physics

A Systematic Resolution Study of $\tau\tau$ Decays at CMS at the LHC

by

Ryan Howard Foote

Submitted to the Department of Physics
on May 20, 2011, in partial fulfillment of the
requirements for the degree of
Bachelor of Science in Physics

Abstract

In this thesis, I perform a systematic resolution study for di-tau pairs at the Compact Muon Solenoid (CMS) experiment at the Large Hadron Collider (LHC) at CERN. I performed this analysis using Monte Carlo simulated events with a Higgs boson which decays into two tau particles with initial mass $m_H = 90 - 500$ GeV/c^2. The two daughter taus were required to then decay leptonically. I determined the dependence of the input mass on the mass resolution and total energy contribution of the electron/muon visible mass peak. For $m_H \leq 120$ GeV/c^2, a mass resolution of $\leq 25\%$ and total energy fraction of $\geq 50\%$ can be achieved.

Thesis Supervisor: Markus Klute
Title: Assistant Professor

Acknowledgments

I would like to thank my thesis advisor Professor Markus Klute. Even with his busy schedule, he was always willing to answer any questions I had and provide me with encouragement. His advice on how to actually write a thesis, as well as his excitement about physics have kept me on course, even on days when I wondered why the hell I ever decided to pursue this major.

I would also like to thank Duncan Ralph and Zach Hynes. Without Duncan's constant presence in the office and both of their willingness to help me fix my code, I probably would have never finished my thesis.

I am also grateful to the contributions and mentoring of Professor Christoph Paus and Professor Steve Nahn. Whether answering questions about life, graduate school, or the perfect mini-basketball freethrow shot, they have always been positive influences on both my academic and personal life.

Additionally I would like to thank Professor Nergis Mavalvala for her support and advice. Having her as my professor for both semesters of Junior Lab was the only reason I survived. Between grilling me on my oral presentations or counselling me on my future career in physics, her presence over the last two years has helped me in incalculable ways.

Finally I would like to thank my family and friends. Without the love and support of my Mom and Dad and my three brothers: Cam, Sean, and Dan, I would not be where I am today. I also owe a debt of gratitude to Kyle Fink, Tommy Gerrity, Grace Taylor, and Adam Tourgee for their unique ability to keep me sane in the face of the nearly insurmountable stress that accompanies an undergraduate degree at MIT.

Contents

Chapter 1

Introduction

Since the time of the Ancient Greeks, man has sought to form an understanding of matter by considering its fundamental building blocks. That goal has not changed, and as modern physicists we call our current understanding of matter the Standard Model. The Standard Model describes the interactions between all of the particles we currently know. Composed of quarks, leptons, and force mediators, our theory of the Standard Model is one of the most complete theories in physics to date. There remain some inconsistencies in our theory, however. For example, we require the existence of a Higgs boson to explain why particles have mass. This particle has yet to be discovered, and to this day exists only as a theoretical construct. There also may exist other particles which indicate "new physics" to be explored. Theories such as supersymmetry and string theory hold the potential to introduce new fundamental particles to our understanding of the world around us.

In order to discover the objects implied by our theories, large particle colliders have been built. The Large Hadron Collider (LHC) is a huge ring 27 km in circumference which accelerates protons to nearly the speed of light. With a center of mass energy of 14 TeV expected in 2012 to 2014, the LHC is the most powerful particle accelerator on the planet. These high energies allow the LHC to produce never-before seen particles such as the Higgs boson. In order to find these particles, huge detectors such as the Compact Muon Solenoid (CMS) are built along the beam path of the LHC at collision points. They record the results of the collisions so that they can be analyzed.

If a Higgs boson were to be created at the LHC, it would decay immediately. By reconstructing the particles from the decay, we can calculate its mass. The Higgs boson can decay by a variety of different channels, and the method of search varies for each one. In this paper, we are concerned primarily with the decay of a Higgs that produces two tau leptons. To successfully discover the Higgs particle that decays via this mode, we must be able to identify τ particles to a high degree of accuracy in our detector.

To that end, this paper analyzes the production of taus via a theoretical Higgs boson decay. Using Monte Carlo simulated data, a systematic study of the visual mass resolution of di-tau states was performed. The mass resolution of the di-tau final states in important because it characterizes the degree of certainty we have on our reconstructed mass values. A low mass resolution does not allow for a complete reconstruction of the initial τ state. For this study, we considered only leptonic τ decays. We also looked at the mass dependence of the resolution for various masses of our parent particles. Good mass resolution for taus is essential to calculating the mass of a Higgs boson that decays via the di-tau mode.

The goal of this paper is to provide a concise yet complete explanation of the $\tau\tau$ resolution study. In Section 2 of this paper we give an overview of the theory of the Standard Model, the Higgs boson, and the τ lepton. We next address the experimental apparatus in Section 3. This covers the LHC and provides an in-depth look at the CMS detector and its constituent parts. In Section 4 we will discuss the identification and reconstruction of the τ in CMS. Finally we will examine the results of our systematic resolution analysis of our taus in Section 5 and Section 6. This paper is intended to be self-contained, however the references should be consulted for additional detail. Also, for all subsequent calculations and equations, our units are such that $\hbar = q = c = 1$.

Chapter 2

Theory

In this section, we will lay the theoretical groundwork necessary to explain the construction of our experimental apparatus as well as the computational approaches utilized for the identification and analysis of the τ lepton. We begin at the broadest scale with an overview of the Standard Model of particle physics. The Standard Model describes the fundamental particles and interactions that correspond to all known matter. This model, however, doesn't provide an explanation as to why the $W^{\pm}$ and Z bosons have mass. We address this in the next section with a description of the Higgs Boson and its implications. Finally, we will discuss in detail the properties and characteristics of the τ particle relevant to our resolution analysis.

2.1 The Standard Model

The Standard Model (SM) describes our current view of particle physics. According to the SM, there are 3 types of elementary particles: mediators, leptons, and quarks. Within each category, there exist varying number of unique particles. Combining these building blocks in specific ways allows us to make up all of the known matter in our universe. For example, a hydrogen atom in a simplified model is a combination of 3 quarks and a lepton. Before we talk any further about composite objects, it is useful to define the properties which identify particles as leptons, quarks, or mediators.

Each lepton is classified by its charge (Q) and its relative mass. An electron for

example has a mass of 511 keV while the corresponding electron neutrino is nearly massless. A break down of the leptons can be seen in Table 2.1. As the table indicates, leptons are naturally organized into 3 different generations, which vary by mass. The 1^{st} generation is the lightest and the 3^{rd} is the heaviest. In total, there are 12 leptons: 6 which make up normal matter and 6 complementary antileptons which make up antimatter.

	ℓ	Q
1^{st} Generation	Electron (e)	-1
	Electron Neutrino (ν_e)	0
2^{nd} Generation	Muon (μ)	-1
	Muon Neutrino (ν_μ)	0
3^{rd} Generation	Tau (τ)	-1
	Tau Neutrino (ν_τ)	0

Table 2.1: The 6 leptons arranged by generation. The table of antileptons is the same except all the signs are reversed. Table adapted from [7].

In much the same was as the leptons, there are 6 "flavors" of quarks. They are classified by their charge (Q) as well and again they fall naturally into 3 generations by their mass differences. As before, a table for the 6 quark flavors can be seen in Table 2.2. Both quarks and antiquarks come in three colors: red, blue, and green. Thus we have a total of 36 quarks in our SM.

	q	Q
1^{st} Generation	Up (u)	$+\frac{2}{3}$
	Down (d)	$-\frac{1}{3}$
2^{nd} Generation	Charm (c)	$+\frac{2}{3}$
	Strange (s)	$-\frac{1}{3}$
3^{rd} Generation	Top (t)	$+\frac{2}{3}$
	Bottom (b)	$-\frac{1}{3}$

Table 2.2: The 6 quark flavors arranged by generation. The table of antiquarks is the same except all the signs are reversed. Table adapted from [7].

Finally we come to the force mediators. For every interaction, there is a mediator. The force carrier for the electromagnetic force is the photon. There are three bosons which mediate the weak force: the W^+, the W^-, and the Z. Our final mediator is the gluon. They carry the strong force between quarks and similarly share the property of color. This fact implies that there are 8 gluons and that they are the only one of the mediators that can not exist as an isolated particle [7]. Technically we should mention the graviton; the force mediator of the gravitational force. However, gravity is not relevant to our analysis, so we will ignore it completely in our understanding of the SM and the remainder of this paper.

Overall we have a SM with 60 elementary particles in it. This may seem a rather large number for our theory, but it accounts for every particle we've discovered with extreme accuracy. As useful as the SM is, there are some drawbacks. It doesn't predict the masses of the quarks and leptons within the theory, for example. Additionally, according to the Glashow-Weinberg-Salam theory we should expect at least one more Higgs boson in our theory to make it complete [7]. The search for this Higgs particle is one of the major goals of the LHC and as such, it is worth while to understand the mechanism by which it arises.

2.2 The Higgs Boson

As mentioned previously, it is necessary for our SM to have a massive Higgs boson. As it stands now, the Higgs is a theoretical scalar boson with spin 0. No other scalar bosons have ever been observed in nature. The Higgs particle was theorized in an effort to explain why our vector bosons (Z and $W^{\pm}$) have mass and our photon does not. The search for the so-called "God Particle" stands to either complete our understanding of the Standard Model, or throw it completely into chaos, depending on whether or not it is successfully discovered.

The Higgs particle arises when we perform a study of spontaneous breaking of local gauge symmetry [8]. We will look at the simplest example of $U(1)$ gauge symmetry. We begin with our complex scalar field $\phi = \frac{1}{\sqrt{2}}(\phi_1 + i\phi_2)$ which is described by the

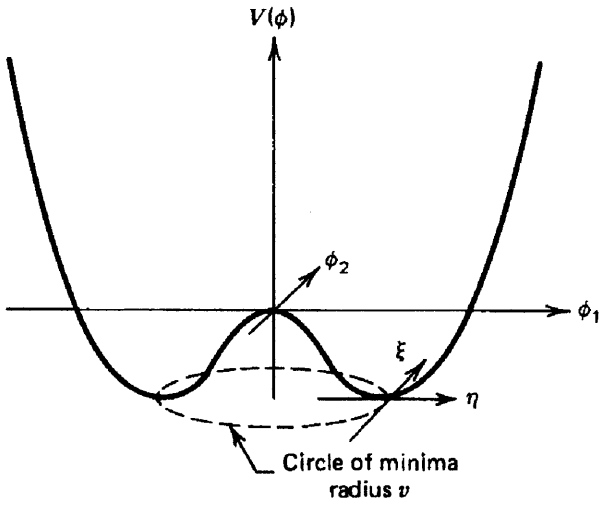

Figure 2-1: Potential $V(\phi)$ for a complex scalar field as described by Equation 2.1. Figure adapted from [8].

Lagrangian:

$$\mathcal{L} = (\partial_\mu \phi)^*(\partial^\mu \phi) - \mu^2 \phi^* \phi - \lambda(\phi^* \phi)^2 \tag{2.1}$$

The potential described by Equation 2.1 is shown in Figure 2-1. It features a circle of minima at $\nu = \sqrt{-\mu^2/\lambda}$ for $\mu^2 < 0$ and $\lambda > 0$. We choose our minimum energy vacuum state to have $\phi_1 = \nu$ and $\phi_2 = 0$.

We now consider our $U(1)$ gauge invariance. This implies that

$$\phi \rightarrow e^{i\alpha(x)} \tag{2.2}$$

which requires us to replace our derivative ∂_μ with a covariant derivative

$$D_\mu = \partial_\mu - ieA_\mu \tag{2.3}$$

Inserting Equations 2.3 and 2.2 into 2.1, we obtain our gauge invariant Lagrangian:

$$\mathcal{L}' = (\partial^\mu + ieA^\mu)\phi^*(\partial_\mu - ieA_\mu)\phi - \mu^2 \phi^* \phi - \lambda(\phi^* \phi)^2 - \frac{1}{4} F_{\mu\nu} F^{\mu\nu} \tag{2.4}$$

We can expand our vacuum state in terms of two new fields η and ξ. Our complex

field can now be written as

$$\phi(x) = \frac{1}{\sqrt{2}}[\nu + \eta(x) + i\xi(x)] \tag{2.5}$$

with $\nu^2 = \phi_1^2 + \phi_2^2 = -\mu^2/\lambda$ as before. This allows us to rewrite our Lagrangian in terms of our new fields η and ξ as

$$\begin{aligned}\mathcal{L}'' = &\frac{1}{2}(\partial_\mu \xi)^2 + \frac{1}{2}(\partial_\mu \eta)^2 - \nu^2\lambda\eta^2 + \frac{1}{2}e^2\nu^2 A_\mu A^\mu \\ &-e\nu A_\mu \partial^\mu \xi - \frac{1}{4}F_{\mu\nu}F^{\mu\nu} + \text{interaction terms}\end{aligned} \tag{2.6}$$

At this point, we pause to understand the Lagrangian described in Equation 2.6. Reading directly off of $\mathcal{L}''$, we can see our theory includes three particles: a massive scalar particle η with mass $m_\eta = \sqrt{2\lambda\nu^2}$, a massive vector A_μ with mass $m_A = e\nu$, and a massless Goldstone Boson ξ with mass $m_\xi = 0$. There are some problems with our theory as it stands, however. First, we notice that our now massive vector A_μ has gained a degree of freedom by way of an additional polarization in the longitudinal direction. Our change of field variables in Equation 2.5 is insufficient to explain this. Second, we recognize the presence of the off-diagonal term $A_\mu \partial^\mu \xi$ in $\mathcal{L}''$. We thus conclude that our Lagrangian fields must not correspond to physical particles.

In order to rectify this inconsistency, we seek a gauge transformation which will eliminate our off-diagonal term. Rewriting our change of field variables to lowest order in ξ, we find

$$\phi = \frac{1}{\sqrt{2}}(\nu + \eta + i\xi) \simeq \frac{1}{\sqrt{2}}(\nu + \eta)e^{i\xi/\nu} \tag{2.7}$$

We can choose a new set of real fields h, θ, A_μ. Substituting them into Equation 2.7 we obtain new expressions for ϕ and A_μ:

$$\phi(x) \rightarrow \frac{1}{\sqrt{2}}(\nu + h(x))e^{i\theta(x)/\nu} \tag{2.8}$$

$$A_\mu \rightarrow A_\mu + \frac{1}{e\nu}\partial_\mu \theta \tag{2.9}$$

We choose $\theta(x)$ such that our field h is real.

Finally we can substitute our new expressions for ϕ and A_μ into our Lagrangian. Calculating we find

$$\mathcal{L}''' = \frac{1}{2}(\partial_\mu h)^2 - \nu^2\lambda h^2 + \frac{1}{2}e^2\nu^2 A_\mu^2 - \lambda\nu h^3 - \frac{1}{4}\lambda h^4 + \frac{1}{2}e^2 A_\mu^2 h^2 + \nu e^2 A_\mu^2 h - \frac{1}{4}F_{\mu\nu}F^{\mu\nu} \tag{2.10}$$

Our theory now stands with only 2 interacting massive particles: a massive scalar h and a massive vector gauge boson A_μ. Immediately we notice that our Goldstone Boson from $\mathcal{L}$ is no longer present. It has been translated into the third degree of freedom for our vector boson by our clever choice of gauge. This spontaneous symmetry breaking of local gauge invariance resulting in a massive vector field and a massive scalar, is in fact the Higgs Mechanism [8].

Now that we understand what the Higgs is, we can being to search for it. The primary modes of production for the Higgs can be seen in Figure 2-2. After creation, the Higgs can decay into a variety of particles. For the purposes of this study, we are concerned solely with the $H \rightarrow \tau\tau$ decay channel. The branching ratio for this process over a range of 50 GeV $< M_H <$ 200 GeV can also be seen in Figure 2-2. In order to investigate this decay however, we must first understand the properties of its daughter product: the τ.

2.3 The τ Lepton

As discussed in Section 2.1 and Table 2.1, the τ lepton is in the third generation leptons. With a mass of 1777 MeV it is by far the heaviest of the charged leptons. Of the three, the e is the only stable particle. The μ has a lifetime of 2.20×10^{-6} s and decays via $\mu \rightarrow e + \bar{\nu}_e + \nu_\mu$. The τ also decays with a lifetime of 2.91×10^{-13} s. Being significantly heavier than the electron ($m_e = 0.5110$ MeV), muon ($m_\mu = 105.7$ MeV), as well as several other mesons, the τ has a variety of decay channels.

It is convenient to classify the decays of the τ into three categories: one prong, three prong, and five prong decays. A one prong decay implies only one charged

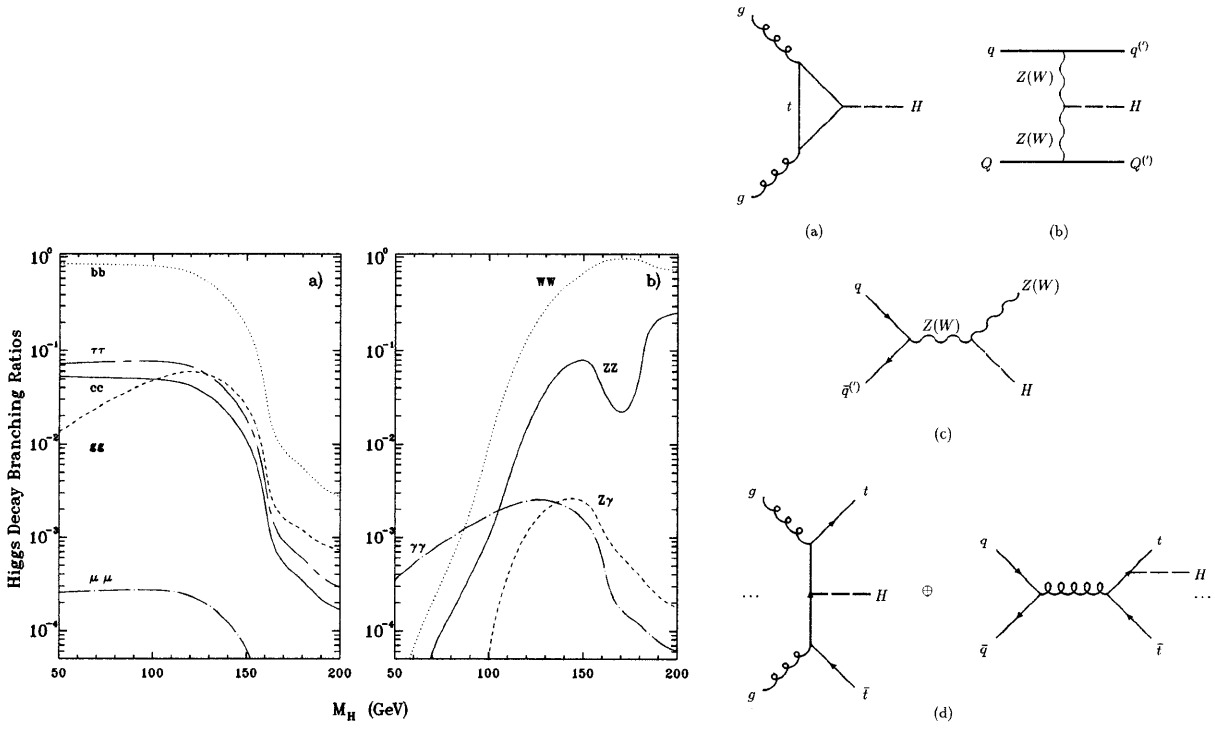

Figure 2-2: Branching ratios for the SM Higgs and primary Higgs production modes at the LHC: **a -** gluon-gluon fusion; **b -** WW - or ZZ - fusion; **c -** associated production with W or Z; **d -** associated production with top quark pairs. Figure adapted from [10].

lepton as one of the decay products. Similarly, the three prong decay and the five prong decay imply three charged leptons and five charged leptons respectively as a part of the decay products. One prong decays account for 85 % of decays, three prong decays compose 15 %, and five prong decays make up < 1 % of all decay events. A breakdown of each category with associated decay rates can be found in Table 2.3.

Decay Channel	**Decay Percentage**
One Prong Contributions	
$h^- h^0 \geq \nu_\tau$	37.05 %
$\ell^- \bar{\nu}_\ell \nu_\tau$	35.20 %
$h^- \nu_\tau$	11.59 %
Total	85.33 %
Three Prong Contributions	
$h^- h^- h^+ \nu_\tau$	9.87 %
$h^- h^- h^+ h^0 \geq \nu_\tau$	5.34 %
Total	14.59 %
Five Prong Contributions	
$h^- h^- h^- h^+ h^+ \geq \nu_\tau$	< 1 %

Table 2.3: Primary decay modes for the τ. h denotes a hadron and ℓ denotes a lepton. Totals include all contributions to each category of decay, not just the main modes shown. Numbers obtained from [6].

Though we recognize that the most prevalent decay mode for taus is a hadronic decay, we will only be considering leptonic decays for the remainder of this paper. Our study focuses uniquely on this process and therefore we do not consider or discuss the topologies and identification algorithms utilized to investigate $\tau-$jets.

Chapter 3

Experiment

Initiation for construction of the Large Hadron Collider (LHC) began with approval by the European Organization for Nuclear Research (CERN) in December 1994. It was originally slated to be assembled in a two stage process so as to assure a constant budget [3]. The first stage, to be operational in 2004, was to have a center of mass energy of 10 TeV. The accelerator was to be upgraded to a 14 TeV center of mass energy for the second stage of it's assembly. However considerable interest in the LHC garnered sufficient financial backing so that in December 1996, approval was given to assemble the experiment directly to the 14 TeV final stage. This project is unique in that it is the first experiment at CERN that has significant contributions from non-member countries like Russia, USA, Canada, India, and Japan. The LHC first began circulating protons in September 2008 and has not yet achieved it's full 14 TeV center of mass energy. It will run at half power through 2012 before an approximate two year shut down to prepare to increase the beam energy to its full amount. The full details of the LHC, its components, and operation can be found in the *LHC Design Report* [3].

3.1 Large Hadron Collider

The LHC has experiments which search for unobserved, rare physics events by accelerating particles around its superconducting 27-km circumference. In order to

increase the chances of detecting a rare phenomenon, a high number of events must be observed. The number of events seen by a particular experiment on the LHC is defined by:

$$N_{event} = \mathcal{L}\sigma_{event} \tag{3.1}$$

where $\mathcal{L}$ is the luminosity of the beam and σ_{event} is the the cross section of the event being observed. As σ_{event} is a term defined by the particle we are accelerating around the ring, we must maximize the luminosity to obtain the highest number of events observed by the detectors.

The luminosity of the beam is dependent upon several beam parameters and is described according to [3]:

$$\mathcal{L} = \frac{N_b^2 n_b f_{rev} \gamma_r}{4\pi\epsilon_n \beta^*} \cdot \left[1 + \left(\frac{\theta_c \sigma_z}{2\sigma^*}\right)^2\right]^{-1/2} \tag{3.2}$$

We notice that our equation can be broken into two parts. In the first is our overall multiplicative factor, where N_b is the number of particles per bunch, n_b is the number of bunches per beam, f_{rev} is the revolution frequency, γ_r is the relativistic gamma factor, ϵ_n is the normalized transverse beam emittance, and β^* is the beta function at the collision point. Our second term is the geometric luminosity reduction factor where θ_c is the full crossing angle at the interaction point, σ_z is the RMS bunch length, and σ^* is the transverse RMS beam size at the interaction point.

In order to obtain the largest number of events observable, we must maximize 3.2. We are limited mechanically by how large we can make factors such as f_{rev} and θ_c, thus we work with N_b. Because it is difficult to produce anti-protons in large quantities, the LHC is primarily a proton-proton beam collider. Each beam has it's own separate magnetic field and vacuum systems. The beams only share a section at each of the interaction regions associated with the experiments on the ring. Additionally the LHC was constructed in the old Large Electron Positron Collider (LEP) tunnels and as such, there is insufficient room to house two separate magnet rings. To solve this problem, specially designed twin-bore magnets hold two sets of

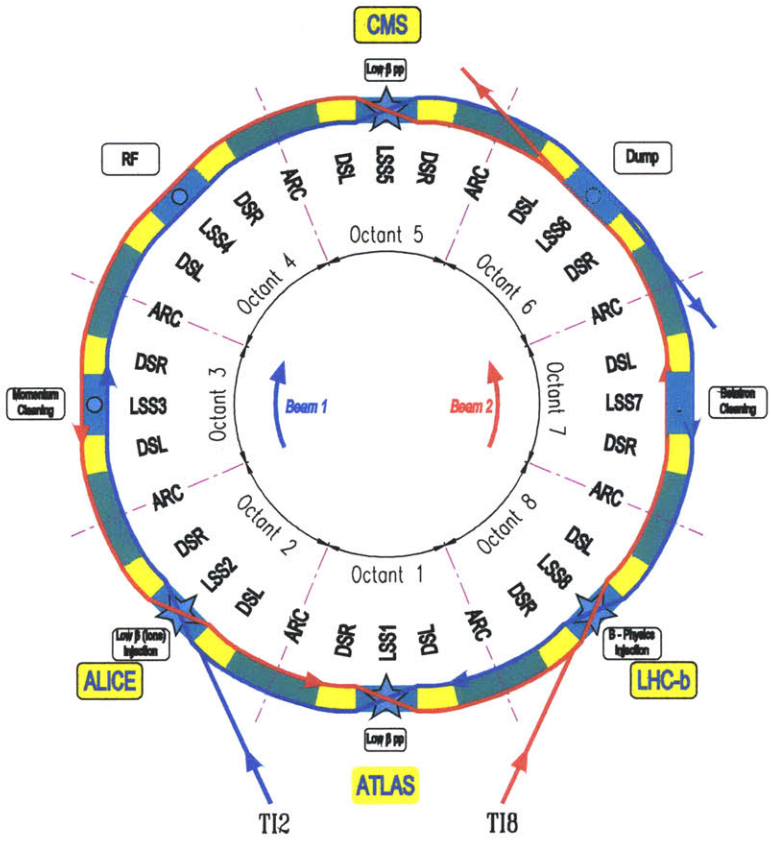

Figure 3-1: Schematic layout of the main LHC ring. Figure adapted from [3].

coils and beam channels. These are then housed within one cryostat system. In order to obtain the final beam energy of 7 TeV, the superconducting magnets must be capable of a peak dipole field of 8.33 T.

The main LHC ring consists of eight curved sections which are labelled octants 1-8 in Figure 3-1. In between the curved regions are straight beam paths intended for the insertion of experiments or other utilities essential for beam operation. Beam crossing points are marked by the four stars and correspond to the location of the experiments. A Toroidal LHC Apparatus (ATLAS) is located on octant 1, ALICE on octant 2, the Compact Muon Solenoid (CMS) on octant 5, and LHC-b on octant 8. Octants 3 and 7 contain two beam collimation systems and octant 4 houses the two RF systems. Additionally, two independent beam dump locations exist along the straight section in octant 6.

The optimal luminosity for each of the experiments is detailed in Table 3.1. Peak luminosity has still not been achieved and will likely not occur until the 14 TeV center of mass energy runs begin around 2014. Full details of the luminosity parameters can be found in [3].

Experiment	Luminosity
ATLAS	10^{34} cm^{-2}s^{-1}
CMS	10^{34} cm^{-2}s^{-1}
LHC-B	10^{32} cm^{-2}s^{-1}
ALICE	10^{27} cm^{-2}s^{-1}

Table 3.1: The optimal luminosities for each experiment on the LHC. Numbers obtained from [3].

3.2 CMS

Shown in Figure 3-2, the CMS detector consists of a 4 T superconducting solenoid along with four sub-detectors: an Electromagnetic Calorimeter (ECAL), a Hadron Calorimeter (HCAL), a silicon tracker, and muon detectors. As discussed in full detail in [5], CMS is specifically designed to have good muon identification, momentum resolution, di-muon mass resolution, electromagnetic energy resolution, and missing energy resolution.

3.2.1 Coordinate System Conventions

The coordinate system for the detector places the origin at the nominal collision point. The x-axis points radially inward towards the center of the LHC, the y-axis points vertically upward, and the z-axis points along the beam line. Cartesian coordinates make particle physics calculations particularly complicated, so a combination of spherical and cylindrical coordinates are used instead. The coordinate r measures the distance from the z-axis. The azimuthal angle ϕ measures the angle between an event and the x-axis in the x-y plane. The polar angle θ similarly measures the angle between an event and the z-axis. θ is infrequently used in our calculations, so we

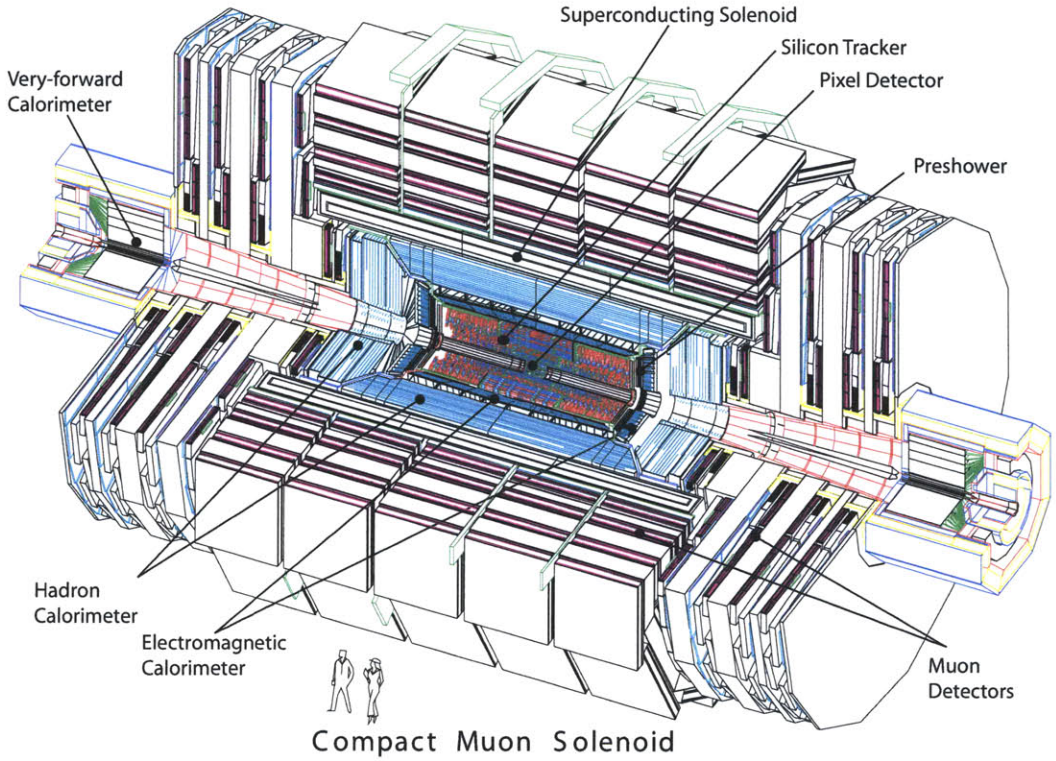

Figure 3-2: An enlarged view of the CMS detector. CMS has a length of 21.6 m, a diameter of 14.6 m, and weighs 12500 tons. Figure adapted from [5].

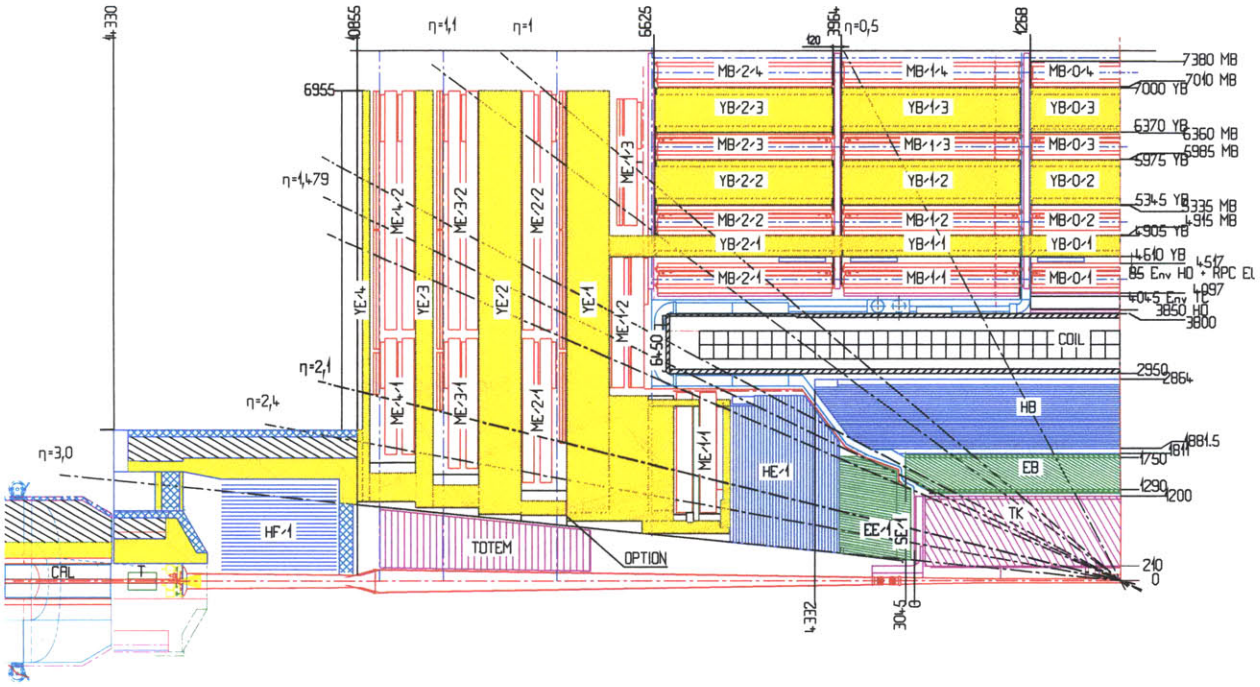

Figure 3-3: A longitudinal one-quarter view of CMS. Figure adapted from [5].

introduce the quantity η called pseudorapidity which is defined as:

$$\eta \equiv -\ln \tan\left(\frac{\theta}{2}\right) \tag{3.3}$$

For reference, a one-quarter longitudinal view of the detector with lines of constant η can be seen in Figure 3-3.

3.2.2 Silicon Strip Tracker and Pixel Detector

As discussed earlier, the results of collisions in the CMS detector are measured by multiple sub-detectors. The innermost sub-detectors located in the inner tracker are the Silicon Strip Tracker (SST) and Pixel Tracker. Their locations in the detector are placed according to the expected particle flux in each region. At a radius of $\approx$ 10cm from the interaction vertex, a particle flux of $\approx 10^7$/s is expected. To accommodate such a high number of particles, pixel detectors are placed around this region. A

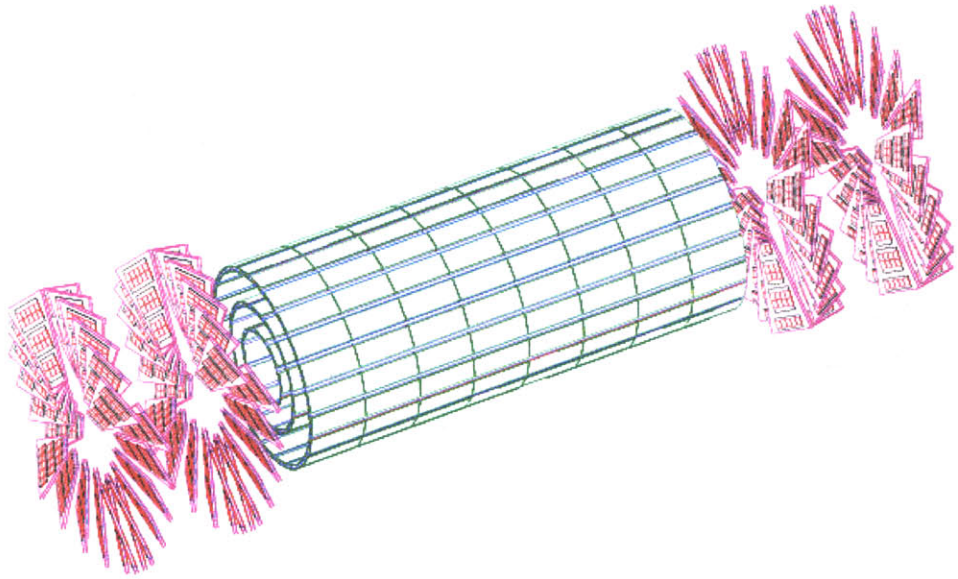

Figure 3-4: Pixel detector locations at CMS. The 3 barrel layers were installed with mean radii of 4.4 cm, 7.3 cm, and 10.2 cm. The endcap discs extend from $r = 6 - 15$ cm. Figure adapted from [5].

diagram of the pixel detector locations within the experiment can be seen in Figure 3-4. There are 3 layers of the pixel detector in the barrel and 2 disks on each of the endcaps. In order to achieve maximum spatial resolution, the pixels were designed to have an area of 100×150 μm^2, giving them an occupancy of about 10^{-4} per pixel per LHC crossing. This yields a resolution of about 20μm for the z measurement and about 10μm for the $r - \phi$.

As we move further from the interaction region, the particle flux diminishes and the SST can be used. They are installed in the intermediate ($20 < r < 55$ cm) and extreme ($r > 55$ cm) regions of the inner tracker. In the intermediate section, silicon microstrip detectors with a cell size of 10 cm $\times$ 80 μm are placed, yielding an occupancy of $\approx 2 - 3\%$ / LHC crossing. The particle flux has sufficiently reduced by the extreme region so larger silicon microstrips with larger pitch values can be used. Their 25 cm $\times$ 180 μm size leads to an occupancy of $\approx 1\%$ / LHC crossing.

The entire SST system is divided into 4 total regions. The intermediate and extreme regions in the barrel correspond to the Tracker Inner Barrel (TIB) and Tracker

Outer Barrel (TOB). The corresponding regions in the endcaps are the Tracker End Cap (TEC) and Tracker Inner Disks (TID). The TIB and TOB have 4 and 6 layers respectively. They also both utilize "stereo" modules, wherein the first two layers for each region are angled so that measurements can be made in both the $r-\phi$ and $r-z$ directions. In both cases, the stereo angle is 100 mrad. This leads to a single-point resolution of 23-34 μm for the TIB and 35-52 μm for the TOB in the $r-\phi$ direction and 23 μm for the TIB and 52 μm for the TOB in the z direction. At the end caps, the TEC contains 9 discs and the TID has 3. As with the barrel, the inner 2 rings of the TID and the 5^{th} ring of the TEC feature stereo modules. The total number of detectors, their thicknesses, and their pitches can be seen in Table 3.2.

Inner Tracker Location	**# of Detectors**	**Thickness (μm)**	**Mean Pitch (μm)**
TIB	2724	320	81/118
TOB	5208	500	81/183
TID	816	320	97/128/143
TEC	2512	320	96/126/128/143
TEC(2)	3888	500	143/158/183

Table 3.2: Breakdown of the Silicon Strip Tracker modules by location. Numbers obtained from [5].

3.2.3 ECAL: Electromagnetic Calorimeter

The Electromagnetic Calorimeter (ECAL) lies directly outside the inner tracker. The ECAL consists of three distinct regions: the barrel region (EB), the endcap region (EE), and the pre-shower device (ES). The barrel region is located at $r = 1.29$ m and the pre-shower device is located directly in front of the endcap region at a longitudinal distance of 3144 mm. The ECAL utilizes lead tungstate ($PbWO_4$) scintillating crystals to detect incident photons and charged particles. The scintillated photons are then measured by avalanche photodiodes (APD) in the barrel region and vacuum phototriodes (VPT) in the endcap region. A transverse view of this subdetector can be seen in Figure 3-5.

The $PbWO_4$ crystals were specially designed for CMS by companies in Russia and

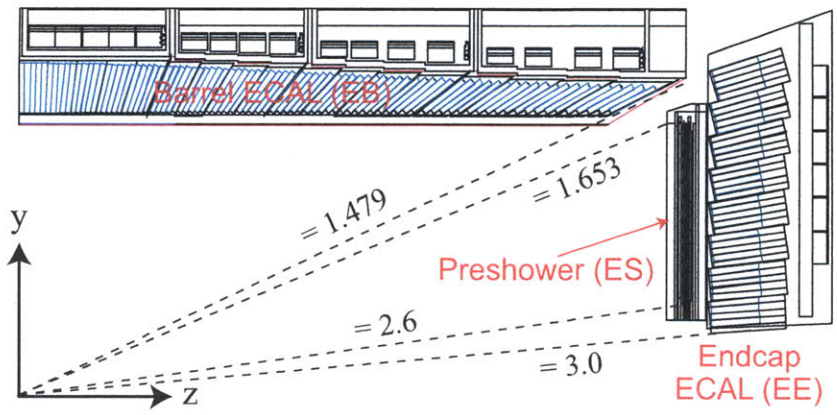

Figure 3-5: Transverse view of the Electromagnetic Calorimeter. Figure adapted from [5].

China. They have a density of 8.3 g/cm^3, a radiation length of $X_0 = 0.89$ cm, and a Molière radius of $R_M = 2.2$ cm. They have a fast scintillation decay time, wherein 80 % of their light is emitted in 25 ns. Additionally, they are radiation hard up to 10 Mrad. These unique crystals allow for very fine granularity under the extreme conditions inside of CMS.

The barrel region of the ECAL contains 36 supermodules, 18 per half barrel. Each supermodule corresponds to 20° in ϕ. Spanning $|\eta| < 1.479$, the barrel region contains 61,200 crystals total. Each crystal is aligned with a 3° tilt with respect to the nominal vertex position. The barrel crystals measure 230 mm long, with a surface area of 22 × 22 mm^2 on their front face and 26 × 26 mm^2 on their back.

Each endcap region of the ECAL detector is separated into two "Dee"s. On each Dee, the crystals are arranged into 5 × 5 "supercrystals" on the $x - y$ grid. In total, one Dee has 3,662 individual crystals. These allow the endcap region to span an eta range from $1.479 < |\eta| < 3.0$. The endcap crystals measure 220 mm in length, with a surface area of 28.62 × 28.62 mm^2 on the front and 30 × 30 mm^2 on the rear.

In front of the endcap region lies the pre-shower device. It covers a fiducial region of $1.635 < |\eta| < 2.6$. The ES operates by placing a layer of lead in front of a silicon strip detector. The incident particles shower when they hit the lead and the trackers measure the deposited energy. Its primary purpose is to identify neutral pions and

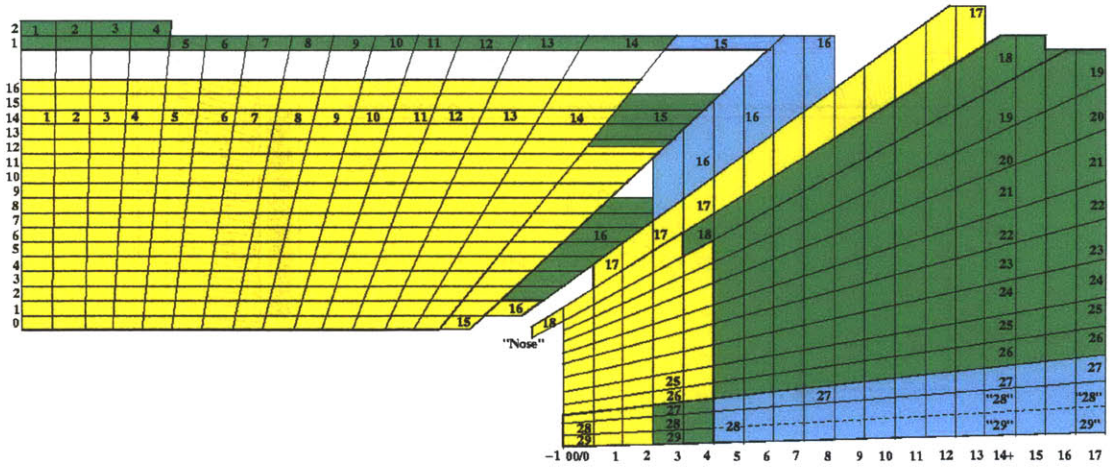

Figure 3-6: Tower mapping in the $r - z$ plane of the HB and HE regions of the Hadronic Calorimeter. Figure adapted from [5].

to provide higher precision position identification for photons and electrons.

3.2.4 HCAL: Hadron Calorimeter

The Hadron Calorimeter (HCAL) lies primarily between the ECAL and the solenoid. It is broken into 4 sections: the barrel region (HB), the endcap region (HE), the forward region (HF) and the outer barrel region (HO). The HCAL measures the energy deposited by hadronic jets and keeps track of missing energy from non-interacting particles such as neutrinos. A diagram of the HCAL can be seen in Figure 3-6.

Each region of the HCAL operates under the same basic principle. Alternating tiles of steel, brass, and plastic scintillator are sandwiched together to record the energy deposited by the hadronic jets. The readouts from the tiles are collected and optically added to tiles along the same line in η. These groupings are called towers. Signal from each tower is then measured by a pixelated hybrid photodiode (HPD) located at the ends of the barrel.

The HCAL is also unique in that it covers a rather large fiducial region. η ranges for each region can be seen in Table 3.3. Having the HF available for large values allows for highly improved measurement of extremely energetic forward jets. Additionally, the HCAL allows for better central shower containment because of the

overlapped HO and HB regions. To account for this, the HO is located outside of the solenoid.

Region	Fiducial Range
HO	$\|\eta\| < 1.26$
HB	$\|\eta\| < 1.4$
HE	$1.3 < \|\eta\| < 3.0$
HF	$2.9 < \|\eta\| < 5.0$

Table 3.3: Fiducial regions for each region of the HCAL. Numbers obtained from[5].

3.2.5 Muon Detectors

Beyond the inner tracker, ECAL, and HCAL lies the superconducting solenoid and muon detector. The solenoid operates at a field of $\approx$ 4 T and at a temperature of $\approx$ 4.6 K. Using almost 5 tons of NbTi, it extends 12.9 m in length and contains 2,168 turns of wire [1]. It also carries a current of 19.5 kA which implies a stored energy of 2.7 GJ. Such a powerful solenoid is necessary to visibly deflect high momentum charged particles as they leave the interaction point.

To measure the momentum of the muons, one must simply measure the deflection from the interaction vertex due to the magnetic fields. However, the track of the muon must be observed to do this. This achieved through the use of three different detectors: drift tube chambers (DT), cathode strip chambers (CSC), and resistive plate chambers (RPC). The locations of these detectors can be seen in Figure 3-7. The DT is utilized in the barrel section because of its low induced neutron background and low residual magnetic field. The CSC and RPC are prominently featured in the endcaps to account for the high muon rate, increased induced neutron background and high magnetic field. Further details about the muon chambers can be seen in [5].

3.2.6 Triggering

As mentioned previously, the LHC is designed to operate at a peak luminosity of 10^{34} $cm^{-2}s^{-1}$. This implies 10^9 events per second incident on the CMS detector. This is

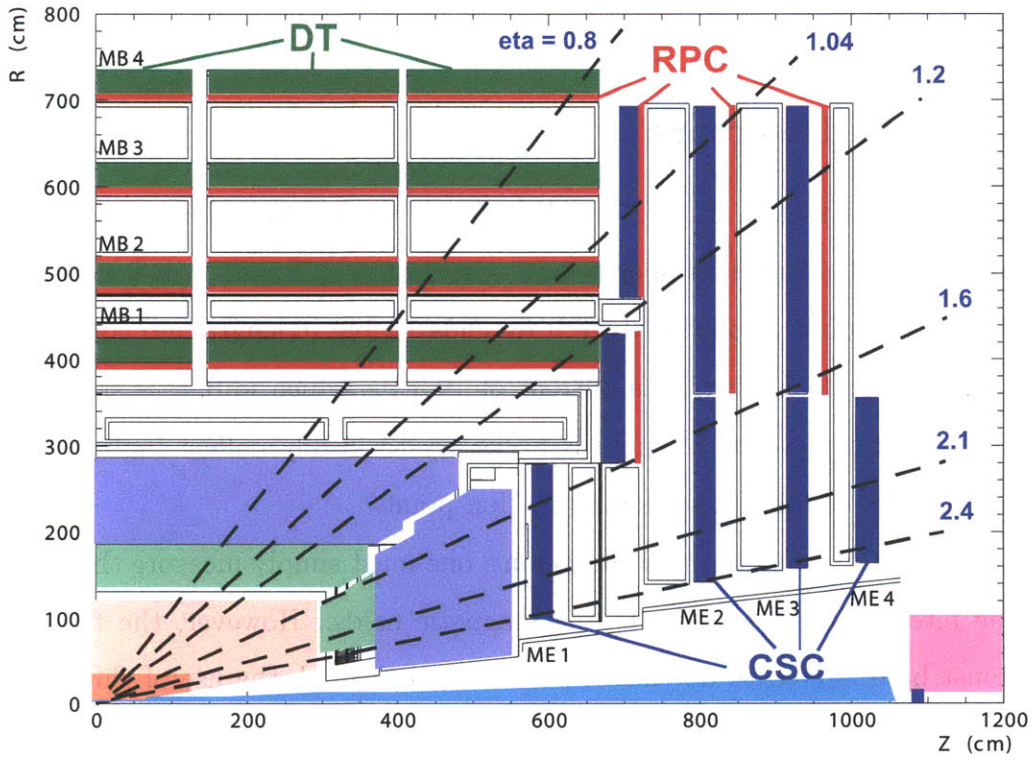

Figure 3-7: One-quarter layout of the muon chambers. Figure adapted from [5].

far more information than can possibly be stored with current computer technology. In fact, the on-line computer farm is limited by an input rate of only 100 Hz. This is a reduction by a factor of 10^7. The method of reduction of data from 10^9 to 10^2 is implemented through triggering. CMS uses two primary triggers: the Level-1 Trigger system (L1) and the High Level Trigger system (HLT). A schematic diagram of the triggering and data acquisition system can be seen in Figure 3-8.

The L1 trigger, as its name would suggest, is the first reduction point for the data. The amount of data that can be stored after an L1 trigger accept is limited by the size of the storage in the pre-shower and tracker buffers. Taking into account the signal propagation delays as well, we find an L1 pipeline data storage time of 3.2 μs [4]. The calculations for each event must be performed in less than 1 μs. In order to keep up with amount of data present in the buffer, the L1 trigger issues a decision and accepts a new event every 25 ns.

Triggering decisions made by the L1 involve the presence of photons, electrons, muons, and jets in given elements of $\eta - \phi$ space. Global sums of both missing and visible E_T as well as p_T or E_T thresholds are also considered when triggering. The L1 also has the ability vary the trigger rates based on individual channel conditions. Overall, a maximum trigger rate of 100 kHz can be achieved by the L1 trigger.

The HLT is intended to reduce the 75 kHz event output rate from the L1 down to 100 events per second. This is first implemented via a series of HLT filters. These filters act on subsets of the data from the detector components to maintain a reasonable system bandwidth. The sum of these filters introduce an overall reduction of the event rate by an order of magnitude.

The majority of the remaining triggering decisions arise from analysis of additional data. Events stored locally in the L1 trigger crates are available to the HLT's. By manipulating the crate data via combinations and topological calculations, a number of further events are triggered. The final event stream reduction down to 100 events per second occurs when the HLT's analyze data from other parts of the detector not initially available to the L1. This includes information from the trackers and full granularity from the calorimeters [4].

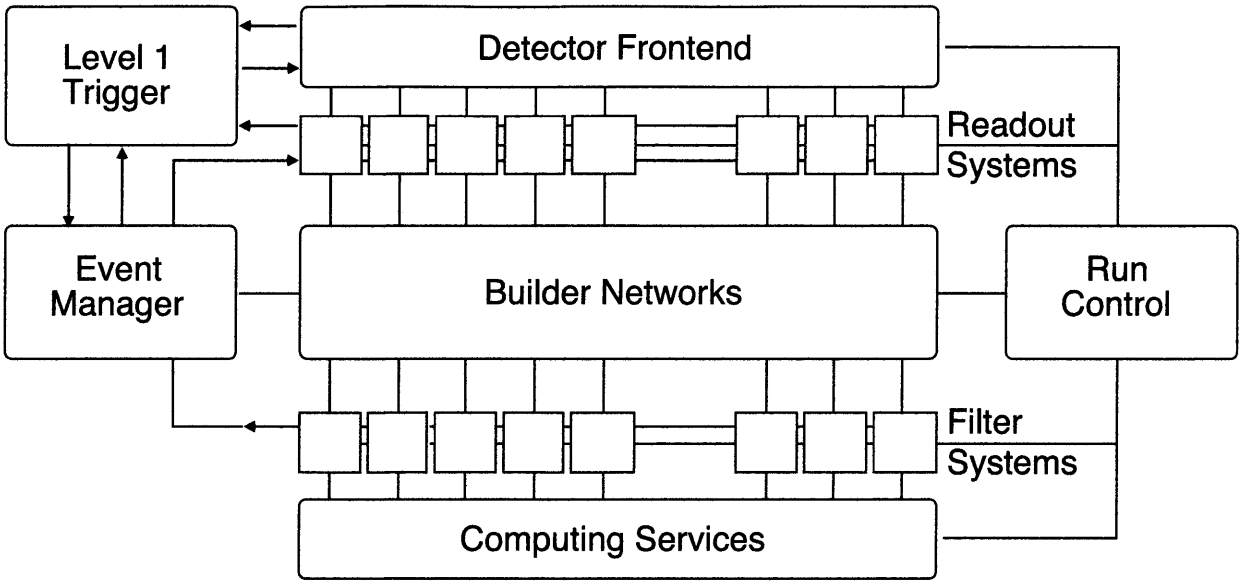

Figure 3-8: Trigger and Data Acquisition system at CMS. Figure adapted from [4].

As we will discuss in the next chapter, both the L1 and HLT triggers play an integral role in finding τ candidate events for further analysis. Once events have been identified as containing a τ particle, reconstruction can begin to determine the invariant mass of the tau.

Chapter 4

τ Identification and Reconstruction

For our mass resolution analysis, we are only concerned with $\tau \rightarrow \ell^- + \bar{\nu}_\ell + \nu_\tau$ decays. As described in Table 2.3, this occurs about 35% of the time. When the decay occurs, the neutrinos leave the detector as missing energy. Therefore, all the information about the parent tau particle is contained within the electrons and muons that result from the decay. In order to identify and reconstruct a tau, we must be able to efficiently recognize electrons and muons in the detector. This is accomplished by implementing specific triggering algorithms in the L1 and HLT systems. Then, by analyzing the data accepted by the triggers, we are able to reconstruct information about the parent taus.

4.1 Electron/Photon Triggering

The electron/photon triggers utilize a 3×3 trigger tower sliding window technique which is consistent for the entire η, ϕ range of the ECAL [4]. The algorithm considers the tower hit by the incident particle and it's 8 nearest neighbors. Transverse energy (E_T) of the electron/photon is measured by combining the E_T in the central tower with the tower that has the largest E_T from one of the four towers that form a "plus" sign with the central tower. Electrons/photons are separated into two different triggering channels: Isolated and Non-Isolated. Non-isolated electrons/photons must pass the following two vetos to trigger:

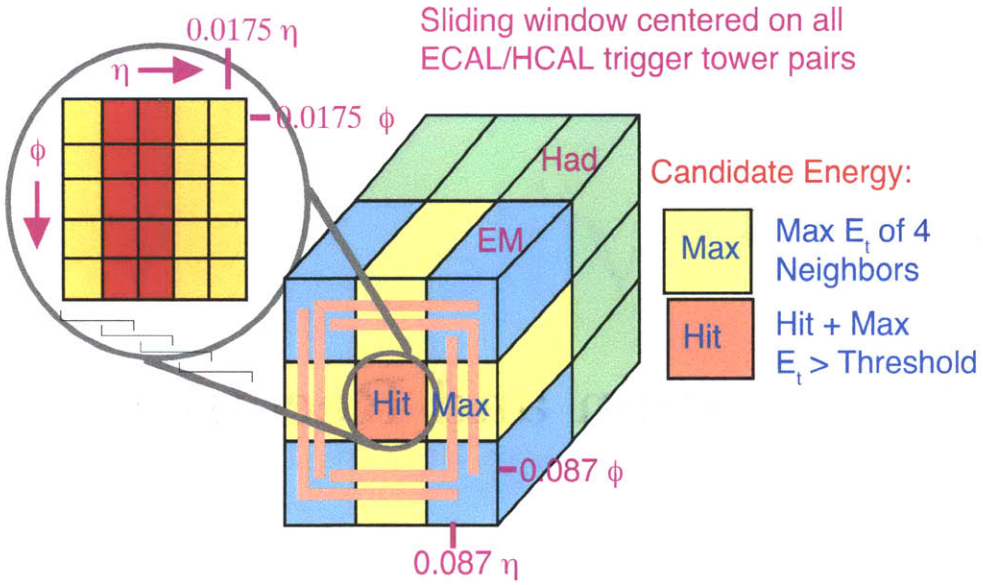

Figure 4-1: Schematic description of the electron/photon trigger algorithm. Figure adapted from [4].

- Fine grain ECAL crystal energy profile (FG Veto)
- HCAL to ECAL energy comparison (HAC veto)

Isolated electrons/photons must pass some additional constraints:

- FG and HAC vetos on *ALL* eight nearest neighbor towers
- One quiet corner where all towers on the corner are below a certain programmable energy threshold

A diagram of the electron/photon triggering algorithm can be seen in Figure 4-1.

The typical energy threshold for the electron/photon trigger is about 30 GeV at high luminosity. Events that trigger are sorted by their E_T and by which 4×4 calorimeter region they are detected in. 95% efficiency is achieved for electrons at 20 GeV and photons at 35 GeV. Thus, particles which deposit most of their energy into the ECAL crystals while satisfying the above triggering criteria are identified and stored as photons/electrons.

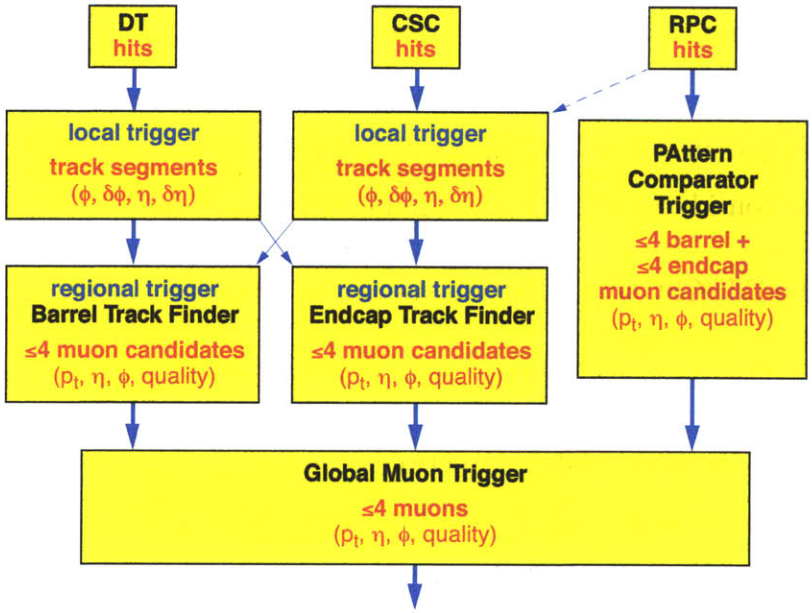

Figure 4-2: Schematic diagram of the data flow for the muon trigger systems. Figure adapted from [4].

4.2 Muon Triggering

As discussed in Section 3.2.5, the muon detector system is comprised of 3 sub-detectors: the Drift Tubes (DT), the Cathode Strip Chambers (CSC), and the Resistive Plate Chambers (RPC). These systems all lie outside of the solenoid. Therefore, the first criteria for muon detection is that the particle must travel through the entire detector while depositing energy in all regions it encounters. When selecting good muon events, the trigger must still be considered. The muon trigger is broken into two trigger sub-systems, with the DT and CSC forming one and the RPC acting as the second. Having two trigger sub-systems is extremely advantageous, as each one contains different information about the muon tracks and background. For example, the charge weighting of the CSC and $\sim$ 400 ns drift time of the DT make that particular sub-system particularly vulnerable to muon radiation, whereas the RPC is not as affected. The individual algorithms for each triggering sub-system are covered extensively in [4]. A diagram of the data flow of the system can be seen in Figure 4-2.

Muon candidacy decisions and analysis of the two sub-systems is performed by the Global Muon Trigger (GMT). Using the logical *AND* and *OR* operations, information from each sub-system can be combined with high efficiency and background rejection. In order to be considered, the potential muon must meet one of two requirements:

- Both the DT/CSC and RPC sub-systems observe the event
- High quality observation of the event in only one sub-system

The GMT performs signal matching between the best 4 muons from each of the DT and CSC systems as well as the best 8 from the RPC detectors. It then passes the overall best 4 muons on to the Global Trigger to be analyzed and recorded.

Chapter 5

Resolution Study

In order to perform our study, a series of Higgs boson datasets must be obtained. Using Pythia 6 [11] along with the TAUOLA package, simulated Higgs events at various masses can be created. Pythia is a Monte Carlo simulator that uses branching ratios and cross sections to randomly generate events that would occur in pp collisions. The TAUOLA package provides the information for simulating τ particle decays. These events are then passed to GEANT4 which simulates the particles interacting with the CMS detector. The CMS reconstruction software (CMSSW) then reconstructs the results of the simulated events. For our analysis, we utilzed CMSSW version 4.1.3. Then, by implementing an EMUAnalysis module, we were able to select only events that featured a $H \rightarrow \tau\tau$ decay with one electron and one muon daughter. The reason why ee and $\mu\mu$ decays aren't considered is to avoid the large background in these channels from Z decays. When we select our electron and our muon in each sample, we also require that the charges of the two particles sum to zero. This accounts for the charge conservation that must be maintained from the $\tau^+\tau^-$ decay.

5.1 Di-tau Mass Reconstruction

When each τ decays, an electron or muon and two neutrinos are produced. As the neutrinos don't interact with the detector at all, their precise energies cannot be determined. However the total transverse energy imbalance can be calculated.

This energy imbalance, or missing transverse energy $\not\!\!E_T$, accounts for all neutrinos in the event. One cannot distinguish between the individual contributions from each neutrino, only the total missing energy can be determined. Therefore, by summing $\not\!\!E_T$ with the energies of the particles detected, one can naively reconstruct the initial mass of the τ. The fraction of the original τ momentum carried by each of the lepton daughters can be calculated in the following way [9],

$$\begin{aligned} p_{T_{Higgs}} &= p_{T_{\tau 1}} + p_{T_{\tau 2}} + \not\!\!p_T \\ x_{\tau_i} &= \frac{p_{T_{lepi}}}{p_{T_{\tau i}}} \\ x_{\tau_1} &= \frac{p_{T_{lep1,x}} \cdot p_{T_{lep2,y}} - p_{T_{lep1,y}} \cdot p_{T_{lep2,x}}}{p_{T_{Higgs,x}} \cdot p_{T_{lep2,y}} - p_{T_{Higgs,y}} \cdot p_{T_{lep2,x}}} \\ x_{\tau_2} &= \frac{p_{T_{lep1,x}} \cdot p_{T_{lep2,y}} - p_{T_{lep1,y}} \cdot p_{T_{lep2,x}}}{p_{T_{Higgs,y}} \cdot p_{T_{lep1,x}} - p_{T_{Higgs,x}} \cdot p_{T_{lep1,y}}} \end{aligned} \tag{5.1}$$

where x_{τ_1}, x_{τ_2} are the momentum fractions of the two τ's carried by the letptons and p_T is the transverse momentum. Once we obtain the values of x_{τ_1} and x_{τ_2}, we can calculate the reconstructed mass of the tau's. This is given by [9]:

$$m_{\tau\tau} = \frac{m_{e\mu}}{\sqrt{x_{\tau_1} x_{\tau_2}}} \tag{5.2}$$

A problem arises when we consider a Higgs which decays and produces two taus "back-to-back". When those τ's decay, the neutrinos from each τ will also exit the detector at $\approx 180°$ to each other. This means that some of the missing momentum gets cancelled out [2]. This can be seen in Equation 5.1. If the two τ's are back to back, then the expressions for the momentum fractions x_{τ_i} become linearly dependent and the denominator becomes equal to zero. Figure 5-1 shows an example of an attempted reconstruction of a $H \rightarrow \tau\tau$ with $m_H = 120$ GeV/c^2. It can be clearly seen in the figure that there is a non-zero contribution to the histogram at zero mass. Additionally, the histogram has a mean peak vale of 81.92 ± 2.02 GeV/c^2 and an RMS value of 54.29 ± 1.43 GeV/c^2. Such a large uncertainty in the peak value does not make for a good estimation of the invariant mass of the di-tau pair. Looking only at

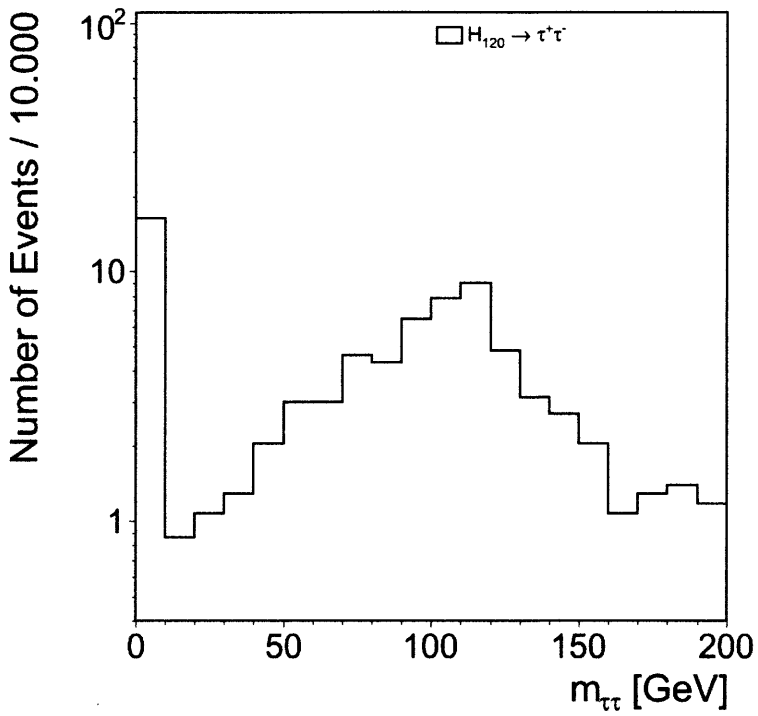

Figure 5-1: Reconstructed $\tau\tau$ for a 120 GeV/c^2 mass Higgs. The back-to-back decay of the di-tau pair makes reconstruction difficult. The peak has a mean value of 81.92 ± 2.02 GeV/c^2 and an RMS value of 54.29 ± 1.43 GeV/c^2.

the reconstructed peak between between 30-180 GeV/c^2 we find a reconstructed di-tau mass of $m_{\tau\tau} = 102.74 \pm 1.39$ GeV/c^2 with an RMS width of 31.86 ± 0.98 GeV/c^2. Additional methods exist for reconstruction of the di-tau mass value, however they are beyond the scope of this paper. We will instead only focus on the mass of the visible decay products, i.e. the electrons and muons.

5.2 Resolution Analysis

13 different Higgs boson input masses were analyzed as a part of our study, with $m_H = 90 - 500$ GeV/c^2. For each input mass value, the visible mass peak of the $e\mu$ pair was calculated and plotted. An example of visible mass peak for a Higgs boson of mass $m_H = 90$ GeV/c^2 can be seen in Figure 5-2.

In order to perform our mass resolution analysis, we must extract information

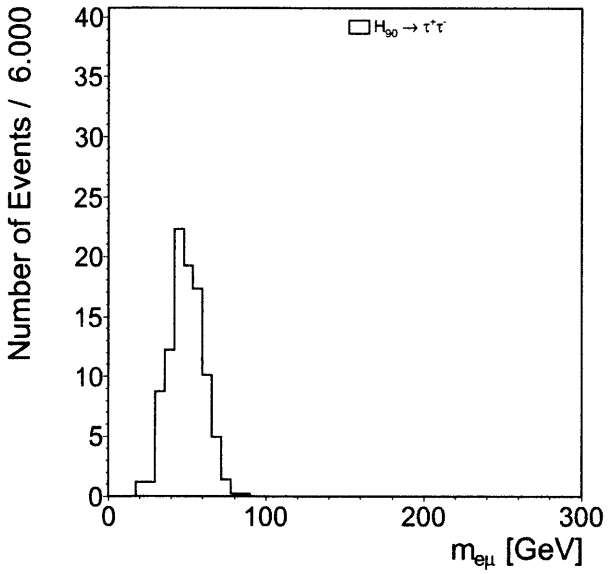

Figure 5-2: Example of an $e\mu$ visible mass peak for a simulated $H \rightarrow \tau\tau$ with $m_H = 90$ GeV/c^2.

about the mean peak location and width of each visible mass peak. Naively observing the shape of the $e\mu$ mass peak in Figure 5-2, we might conclude that a Gaussian distribution would best fit the data. Performing such a fit on our data yields a result similar to that seen in Figure 5-3. Visually, the data does not appear to be Gaussian. If perhaps a second Gaussian were included, it might better fit the simulated results. When one considers the reduced chi-squared value of $\chi^2/\text{ndf} = 10.87$ it becomes clear that a Gaussian fit is not the best choice. Instead of trying to model the data then, we took the mean value to be the average of the x-values weighted by the number of events per bin. The width of the peaks are taken to be their root mean squared (RMS) values. We measured these for each histogram produced and used the results to complete our analysis.

The width of our visible mass peaks corresponds to uncertainty of our mean mass value. In order to precisely identify the total mass attributed to the electrons and muons produced in the decay, we want our width to be as small as possible. Large uncertainty in our visible mass peak will propagate when used to calculate the reconstructed mass for the parent τ. Thus we sought to determine whether there was

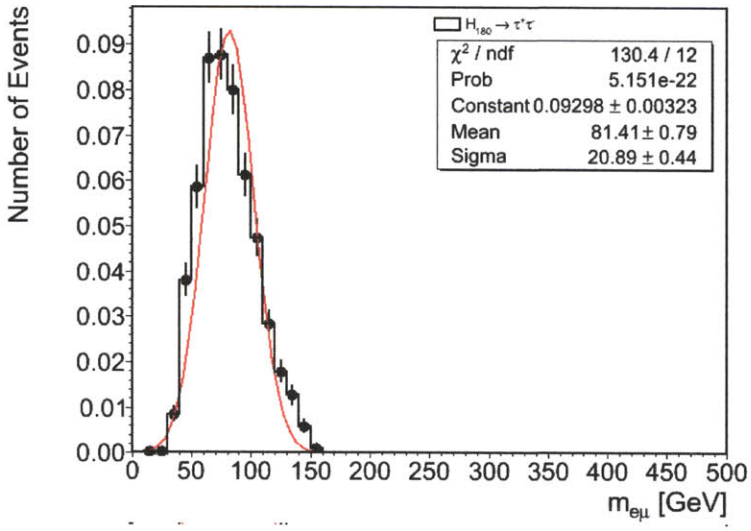

Figure 5-3: Example of a poor Gaussian fit to the $e\mu$ visible mass peak for a simulated $H \rightarrow \tau\tau$ with $m_H = 180$ GeV/c^2.

a dependence between the original Higgs decay and the RMS width of the resulting visible mass peak. For each Higgs mass, the RMS value of the peak was divided by the mean peak position value. This was then plotted against the input mass of the parent Higgs boson. The resulting plot can be seen in Figure 5-4.

We notice almost immediately that the resolution of the visible mass peak degrades as we increase the mass of our initial Higgs boson. For $m_H = 90$ or 100, the uncertainty in the visible peak value is $\sim$ 20%. As the input mass increases, the uncertainty approaches $\sim$ 45%. An uncertainty of $\sim$ 20% already presents a great degree of difficulty in terms of separation of the signal from the background [2]. The data implies that our analysis favors a lower mass Higgs boson. At higher masses then, another method must be employed to improve the resolution.

We continue our analysis by looking at the mean peak value at each different Higgs mass. The total energy of the initial Higgs boson must be conserved. When it decays, its total energy gets divided evenly between the τ's. However, when each τ decays the energy does not get evenly distributed between the lepton and the two neutrinos. As discussed previously, a precise value of $\not{E}_T$ can be difficult to calculate based on the kinematics of the initial Higgs decay. It is therefore much easier to

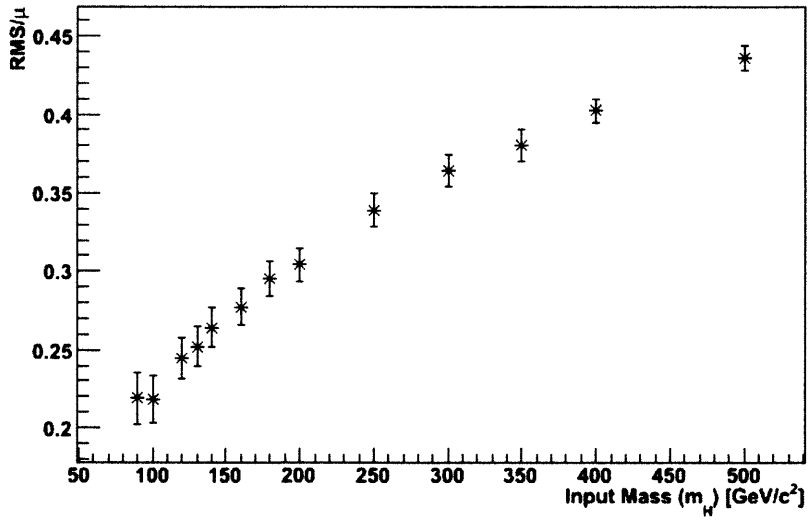

Figure 5-4: Ratio of RMS width to mean peak position plotted against initial Higgs mass. This plot shows the degradation of the visible mass resolution for increasing m_H.

measure the total energy of the visible particles as observed by the detector. It would follow then, that a more successful di-tau reconstruction would occur when more of its initial momentum is transferred to the leptons than the neutrinos. By plotting the ratio of the mean peak value to the initial Higgs mass against the Higgs mass, we were able to observe the relationship between the input mass and the mass of the visible decay products. Said relationship can be observed in Figure 5-5.

According to Figure 5-5, as the input mass of the Higgs boson increases, the overall fraction of the initial energy decreases. For $m_H \leq 120$ GeV/c^2, the $e\mu$ visible mass peak accounts for over 50% of the input rest mass of the parent Higgs. At values of $m_H > 120$ GeV/c^2, we observe the fraction decline from 50% down to $\sim$ 35% at $m_H = 500$ GeV/c^2. When we consider that $\sim$ 65% of the remaining energy is "missing" and that some of that $\not\!\!E_T$ is cancelled out by the back-to-back phenomenon discussed earlier, it becomes impossible to directly reconstruct the invariant mass of the initial τ pair. Considering this fact, we again infer that our analysis technique is best suited for lower mass Higgs boson decays.

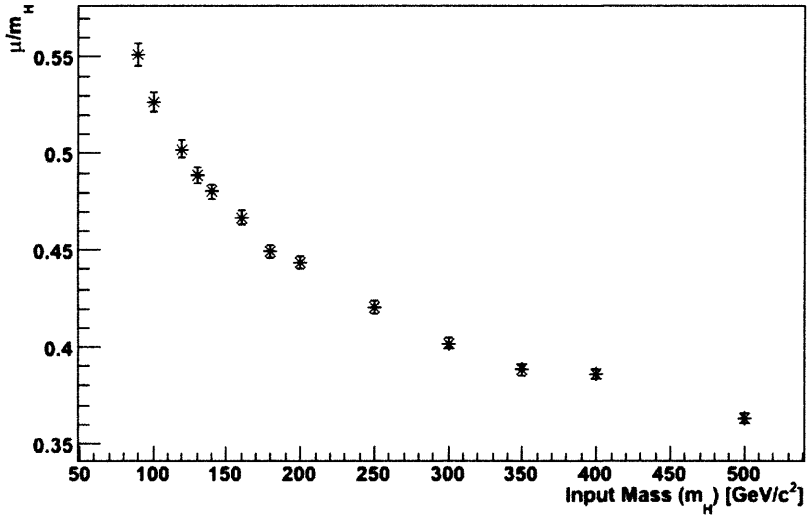

Figure 5-5: Ratio of the mean peak position to the input mass plotted against initial Higgs input mass. This plot shows a reduced fraction of the initial energy in the visible mass decays for increasing m_H.

Chapter 6

Conclusion

Through our mass resolution study, we have encountered first-hand the difficulties associated with a Higgs boson that decays via two τ particles. Our investigation of the properties of the mean peak value and RMS width of the $e\mu$ visual mass peak implied that our analysis is best suited for a low mass Higgs. For a search for the Higgs boson via a di-tau leptonic decay, the mass resolution and overall fraction of the total energy of the visual decay products is maximized at lower values of $m_H \leq 120$ GeV/c^2. In this regime, a resolution of $\leq 25\%$ and fractional energy of $\geq 50\%$ can be attained.

This realm of possible Higgs decay modes only accounts for a small portion of the total search. As mentioned in Section 2.3, the τ particle decays hadronically $\sim 65\%$ of the time. Analysis of this decay mode requires a completely different triggering procedure to obtain events, as well as a drastically different approach to reconstruction techniques. The Higgs boson can also decay into particles other than two τ's, which requires different consideration all together. In this sense, this thesis is a very limited study in one particular facet of the search for the so-called "God Particle". The discovery of such a particle has profound implications for the future of physics. Either its discovery will complete our picture of the Standard Model of physics, or its non-existence will launch us into an exciting and unknown future in which we try to find a new model to explain how matter acquires mass.

Bibliography

[1] *The CMS magnet project: Technical Design Report.* Technical Design Report CMS. CERN, Geneva, 1997.

[2] A.Elagin P.Murat A.Pranko A.Safonov. A new mass reconstruction technique for resonances decaying to $\tau\tau$. *arXiv:1012.4686v2 [hep-ex]*, 2011.

[3] Oliver Sim Brüning, Paul Collier, P Lebrun, Stephen Myers, Ranko Ostojic, John Poole, and Paul Proudlock. *LHC Design Report.* CERN, Geneva, 2004.

[4] The CMS Collaboration. *CMS TriDAS project: Technical Design Report, Volume 1: The Trigger Systems.* Technical Design Report CMS.

[5] The CMS Collaboration. *CMS Physics Technical Design Report Volume I: Detector Performance and Software.* Technical Design Report CMS. CERN, Geneva, 2006.

[6] K. Nakamura et al. (Particle Data Group). The review of particle physics. *J. Phys. G 37, 075021*, 2010.

[7] D. Griffiths. *Introduction to Elementary Particles.* John Wiley & Sons, New York, USA, 1987.

[8] Francis Halzen and Alan D. Martin. *Quarks and Leptons.* John Wiley & Sons, 1985.

[9] Markus Klute. A study of the weak boson fusion, with $h \rightarrow \tau^+\tau^-$ and $\tau \rightarrow e(\mu)\nu_{e,(\mu)}\nu_\tau$. Technical Report ATL-PHYS-2002-018, CERN, Geneva, Mar 2002.

[10] Zoltn Kunszt, S Moretti, and William James Stirling. Higgs production at the lhc: an update on cross sections and branching ratios. (hep-ph/9611397. CAVENDISH-HEP-96-20. DFTT-95-34. DTP-96-100. ETH-TH-96-48), Nov 1996.

[11] Torbjorn Sjostrand, Stephen Mrenna, and Peter Skands. Pythia 6.4 physics and manual. *JHEP*, 0605:026, 2006.